ADVANCED FUNCTIONAL MATERIALS
www.afm-journal.de

Decoupling Substitution Effects from Point Defects in Layered Ni-Rich Oxide Cathode Materials for Lithium-Ion Batteries

Leonhard Karger, Svetlana Korneychuk, Sabrina Sicolo, Hang Li, Wessel van den Bergh, Ruizhuo Zhang, Sylvio Indris, Aleksandr Kondrakov, Jürgen Janek, and Torsten Brezesinski**

Ni-rich $LiNi_xCo_yMn_zO_2$ cathode materials offer high practical capacities and good rate capability, but are notorious for being unstable at high state of charge. Here, a series of such layered oxides with nickel contents ranging from 88 to 100 mol% is fabricated by sodium-to-lithium ion exchange, yielding materials devoid of $Ni^{\bullet}_{Li}$ substitutional defects. Examining the initial charge/discharge cycle reveals effects that are specifically caused by transition-metal substitution, which would otherwise be obscured by changes in lithium-site defect concentration. Lowering the nickel content helps to stabilize the high-voltage regime, while simultaneously negatively affecting lithium diffusion. *Operando* X-ray diffraction indicates mitigation of volume variation during cycling and transition toward solid-solution behavior with sufficiently high cobalt and manganese contents, thus providing an explanation for the increased stability. The interplay between transition-metal substitution, kinetic hindrance, and solid-solution behavior may be a result of local inhomogeneities due to lithium-vacancy pinning, which is further elucidated through density functional theory calculations. Overall, this work sheds new light on the effects of manganese and cobalt incorporation into the transition-metal layer and their conjunction with $Ni^{\bullet}_{Li}$ defects.

1. Introduction

Ni-rich cathode active materials (CAMs) of $LiNi_xCo_yMn_zO_2$ (NCM/NMC) or $LiNi_xCo_yAl_zO_2$ (NCA) type are at the forefront of commercial high-energy-density lithium-ion batteries (LIBs).[1] Although similar capacities can be achieved with different generations of NCMs, increasing the nickel content lowers the cutoff potential at which high specific capacities (>200 mAh g^{-1}) are attainable.[2] However, these Ni-rich CAMs, particularly $LiNiO_2$ (LNO), are notorious for their instability, especially due to degradation at a high state of charge (SOC). The latter has been linked to mechanical degradation resulting from anisotropic volume changes, oxygen release, and surface degradation upon cycling.[3–10]

Intrinsic to all Ni-rich NCMs produced by solid-state synthesis are $Ni^{\bullet}_{Li}$ substitutional defects, sometimes also termed

L. Karger, W. van den Bergh, R. Zhang, A. Kondrakov, J. Janek, T. Brezesinski
Battery and Electrochemistry Laboratory (BELLA)
Institute of Nanotechnology
Karlsruhe Institute of Technology (KIT)
Herrmann-von-Helmholtz-Platz 1, 76344 Eggenstein-Leopoldshafen, Germany
E-mail: juergen.janek@kit.edu; torsten.brezesinski@kit.edu

The ORCID identification number(s) for the author(s) of this article can be found under https://doi.org/10.1002/adfm.202402444

[+]Present address: School of Advanced Materials, Shenzhen Graduate School, Peking University, Shenzhen 518055, China

DOI: 10.1002/adfm.202402444

S. Korneychuk
Institute of Nanotechnology
Karlsruhe Institute of Technology (KIT)
Herrmann-von-Helmholtz-Platz 1, 76344 Eggenstein-Leopoldshafen, Germany

S. Korneychuk
Karlsruhe Nano Micro Facility (KNMFi)
Karlsruhe Institute of Technology (KIT)
Herrmann-von-Helmholtz-Platz 1, 76344 Eggenstein-Leopoldshafen, Germany

S. Sicolo, A. Kondrakov
BASF SE
Carl-Bosch-Str. 38, 67056 Ludwigshafen, Germany

H. Li[+], S. Indris
Institute for Applied Materials – Energy Storage Systems (IAM-ESS)
Karlsruhe Institute of Technology (KIT)
Hermann-von-Helmholtz-Platz 1, 76344 Eggenstein-Leopoldshafen, Germany

J. Janek
Institute of Physical Chemistry & Center for Materials Research (ZfM/LaMa)
Justus-Liebig-University Giessen
Heinrich-Buff-Ring 17, 35392 Giessen, Germany

off-stoichiometry, lithium deficiency,[11,12] or "Ni/Li intermixing", referring to antisite defects, which can occur in the presence of manganese but not in close-to-stoichiometric LNO.[13,14] The origin of these defects lies in the similar ionic radii of Ni^{2+} (r = 0.69 Å) and Li^{+} (r = 0.76 Å),[15] along with the need for strongly oxidizing conditions, causing incomplete layer separation.[16,17] For charge compensation, each $Ni_{Li}^{\bullet}$ defect is accompanied by the presence of a reduced nickel cation in the transition-metal layer, which according to Kröger-Vink notation is represented by $Ni_{Ni}^{'}$.[18] However, for simplicity, we only mention $Ni_{Li}^{\bullet}$ when referring to the combination of $Ni_{Li}^{\bullet}$ and $Ni_{Ni}^{'}$ defects hereafter.

The extent to which these point defects occur is related to the chemical composition. For example, upon increasing the nickel content from 80 to 100 mol% in the solid solution $LiNi_xCo_yO_2$, Caurant et al. found an increase in lithium deficiency from 6 to 10%.[12] Although improvements have been made to the calcination protocols, such that even $Ni_{Li}^{\bullet}$ defect concentrations as low as 1.6% are accessible by conventional solid-state synthesis,[19,20] the problem of convolution of Ni-site substitution with cobalt, manganese, or other metal species with changes in the fraction of $Ni_{Li}^{\bullet}$ defects persists. This makes the correlation between transition-metal site substitution (or doping) and diffusion properties (kinetics) ambiguous, as the effects seen may also originate from differences in $Ni_{Li}^{\bullet}$ concentration.[12] For example, Cui et al. faced this problem when studying the individual effects of modifying LNO with 5% cobalt, manganese, or aluminum. They found poor diffusivity after manganese incorporation and fast lithium diffusion in the case of cobalt, which increases and decreases the fraction of $Ni_{Li}^{\bullet}$ defects, respectively.[21] Therefore, it is experimentally very challenging to separate substitution effects in the transition-metal site from those induced by $Ni_{Li}^{\bullet}$ defects.[22] Nevertheless, understanding the individual contributions to key properties, such as lithium diffusion, lattice parameter changes, and (electro)chemical stability, independent of other factors, such as particle size or $Ni_{Li}^{\bullet}$ defects, is crucial for designing new generations of advanced CAMs. Especially with the emergence of single-crystalline cathodes for improving stability and tap density, realizing sufficiently fast lithium diffusion (mobility) gains momentum.[23–26]

Herein, we attempt to separate the contribution due to cobalt and manganese substitution from $Ni_{Li}^{\bullet}$ defects by employing a recently developed ion-exchange synthesis, yielding $Ni_{Li}^{\bullet}$-free CAM.[27,28] Specifically, a series of NCM materials with varying nickel content was fabricated by sodium-to-lithium ion exchange with the objective to prevent $Ni_{Li}^{\bullet}$ defect formation. Substitution with cobalt and manganese helps to stabilize the high-voltage regime by smoothening the structural transition at high SOC and lowering the overall volume variation. However, there is a trade-off as lowering the nickel content proves detrimental to the lithium diffusion, causing capacity loss due to incomplete relithiation of CAM. With regard to the first-cycle efficiency, ion-exchanged NCM95 (with Ni:Co:Mn molar ratio of 95:4:1) is found to exhibit the lowest cumulative capacity loss among all materials tested in this work.

2. Results and Discussion

The ion-exchange method relies on a perfectly layered "parent" sodium metal oxide. In the case of LNO, this material is $NaNiO_2$ (NNO), which adopts a distorted (monoclinic) $C2/m$ phase at room temperature. In contrast, $NaNi_xCo_yMn_zO_2$ (Na-NCM) materials with $x \leq 0.8$ have been reported to adopt an $R{-}3m$ structure.[29] The synthesis of Ni-rich Na-NCMs is conducted according to an adaption of a previously reported method.[27] In short, co-precipitated hydroxide precursor CAM (pCAM) particles and NaOH are heated at 300 °C in an oxygen atmosphere to remove crystal water and improve wetting, followed by calcination of the premix at 700 °C.

2.1. Sodium Trapping in Single-Crystalline, Ion-Exchanged NCM

The as-synthesized Na-NCM90 (with Ni:Co:Mn molar ratio of 90:5:5) was investigated by powder X-ray diffraction (PXRD), as shown in **Figure 1a**. Corresponding structural parameters determined by Rietveld refinement analysis are given in **Table 1**. PXRD indicates the presence of two phases with space groups $C2/m$ and $R{-}3m$ in a ratio of 84:16 by weight. The structural parameters of the individual phases agree with those reported in the literature.[27,30] However, β is slightly smaller compared to NNO, and the a and b lattice parameters of the monoclinic phase are decreased and increased, respectively. As shown for the Co-doping of NNO, for example, this is indicative of less monoclinic distortion with transition-metal substitution.[31] Therefore, the presence of two phases is not necessarily a sign of separation into Na-NCM and NNO, but rather suggests local inhomogeneities. With regard to the hexagonal phase of Na-NCM90, we find an overall larger unit-cell volume compared to Na-NCM85 (reference from literature).[30]

Next, the Na-NCM90 was subjected to ion exchange and probed again using PXRD. As shown in Figure 1b, two phases are observed, both of which can be indexed to the $R{-}3m$ space group. The main phase corresponds to the ion-exchanged material (IE-NCM90), and the lattice parameters agree well with literature results for IE-NCM and NCM produced by solid-state synthesis.[29,32] The second phase exhibits a peak at the 003 ($R{-}3m$) or 001 position ($C2/m$) of Na-NCM90, and we therefore assign it to sodium-containing (only partially ion-exchanged) domains, likely located in the particle bulk. However, the interlayer spacing is slightly expanded compared to the parent material, which agrees with a previous in situ analysis of the reaction mechanism.[27] The refined weight ratio of these two phases is 95:5, indicating incomplete conversion when using Na-NCM90 as the precursor. This could be a result of too large primary particles (grains) and associated sodium trapping due to poor diffusion.

The morphology and structural attributes of the as-synthesized IE-NCM90 were studied by (scanning) transmission electron microscopy [(S)TEM] of focused-ion beam (FIB)-cut lamellae. The high-angle annular dark field (HAADF) image in **Figure 2a** reveals the presence of monolithic particles with sizes ranging from 1 to 8 µm in diameter. Some particles show signs of cracking, which appears to occur parallel to the sodium/lithium layer, as can be seen in Figure 2b,c,h,i. Small (≈1 µm, see Figure 2b–g) and large particles (≈8 µm, see Figure 2h–m) were examined by energy-dispersive X-ray spectroscopy (EDS). Those imaged in Figure 2 exhibit a uniform distribution of nickel and cobalt, while manganese is present in the bulk, but also segregates at the

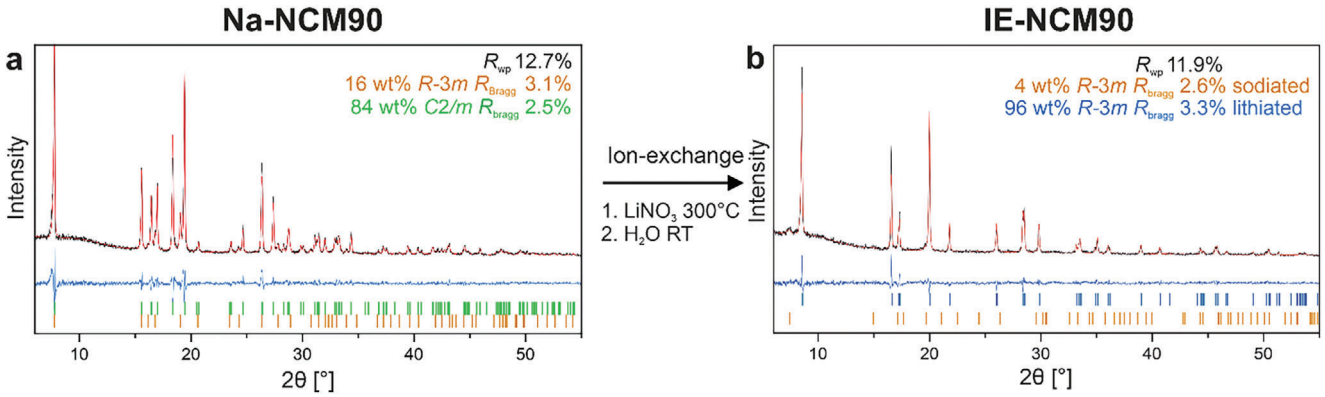

Figure 1. PXRD patterns and Rietveld refinement plots for a) Na-NCM90 and b) IE-NCM90.

Table 1. Structural parameters determined by Rietveld refinement for Na-NCM90, NNO, Na-NCM811, and IE-NCM90.

Sample	Phase	wt.%	R_{wp} [%]	R_{Bragg} [%]	*a* [Å]	*b* [Å]	*c* [Å]	*β* [°]	*V* [Å^3]
Na-NCM90	*C*2/*m*	84	12.7	3.1	5.2847(3)	2.8536(2)	5.5686(4)	110.100(9)	78.86(1)
	R−3*m*	16		2.5	2.9510(4)	–	15.7024(56)	–	118.42(5)
NNO[27]	*C*2/*m*	100	–	2. 7	5.3173(1)	2.8424(1)	5.5789(1)	110.485(1)	78.99(1)
Na-NCM811[30]	*R*−3*m*	100	12.6	–	2.9309(1)	–	15.776(8)	–	117.36(7)
IE-NCM90	*R*−3*m*	96	11.9	3.3	2.8763(2)	–	14.1915(10)	–	101.68(1)
	R−3*m*	4		2.6	2.8617(15)	–	16.3245(333)	–	115.77(47)

surface. This could be due to the formation of Mn^{4+} during the pre-annealing. Because of the high oxidation state, Mn^{4+} is expected to diffuse slower in a solid-state reaction. In the following, the atmosphere in this step of the synthesis was thus changed from oxygen to argon. In the large particle, residual sodium is clearly observed by EDS, which is not evenly distributed in the bulk, but is present in enriched domains of several hundred nanometers in size. Within such a domain, layer bending is apparent, as can be seen in Figure 2i. This is probably a result of high strain due to the co-presence of lithium and sodium in adjacent phases. These sodium-enriched domains are likely visible—in the form of the 5% impurity phase—in the PXRD pattern in Figure 1b. Contrary to previous findings on IE-LNO particles, no cracking parallel to the stacking direction is observed.[27] This points toward an increase in mechanical stability resulting from the transition-metal substitution. The small particle also contains some residual sodium. As evident from Figure 2g, it is located within a small volume fraction of the particle. This means that the bulk is largely free of sodium, and further suggests that smaller particles allow for more efficient sodium-to-lithium ion exchange.[28]

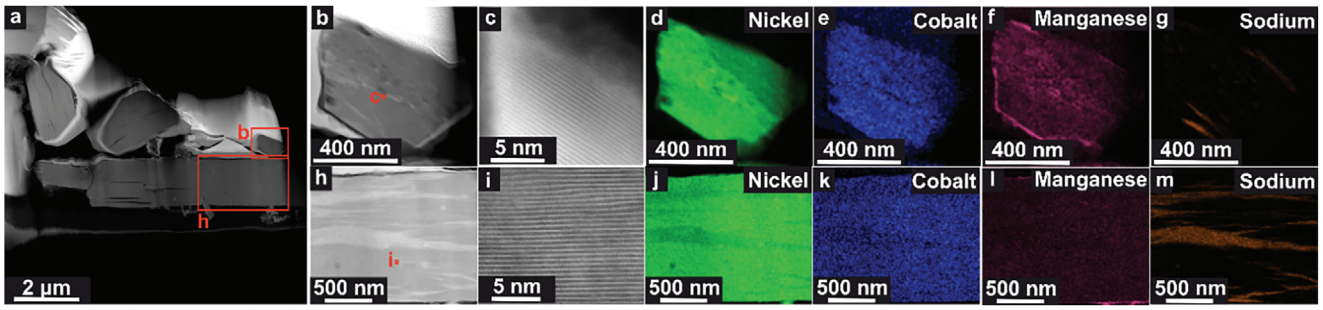

Figure 2. (S)TEM analysis of FIB-prepared IE-NCM90 with areas probed by EDS indicated by red rectangles in (a). b,h) Higher-magnification HAADF images of the regions of interest, and c,i) high-resolution images of the areas highlighted in red in panels (b) and (h). d–g, j–m) EDS maps for nickel, cobalt, manganese, and sodium.

Table 2. Results from ICP-OES (normalized to the cumulative amount of nickel, cobalt, and manganese).

Sample	Li [%]	Na [%]	Ni [%]	Co [%]	Mn [%]	W [%]	O [%]
IE-LNO-W	93.1	1.2	100	0	0	0.40	208.5
IE-NCM95-W	92.9	1.9	93.5	4.5	2.0	0.50	219.1
IE-NCM90-W	93.2	1.2	90.1	4.9	5.0	0.52	217.7
IE-NCM88-W	93.7	1.4	87.3	4.7	8.0	1.06	219.2

IE-NCM90 was also tested electrochemically in LIB half-cells at a C/10 rate (with 1C = 200 mA $g_{CAM}{}^{-1}$) in the potential window of 3.0–4.3 V versus Li^+/Li (see Figure S1, Supporting Information). Specific capacities of q_{ch} = 209 mAh $g_{CAM}{}^{-1}$ and q_{dis} = 163 mAh $g_{CAM}{}^{-1}$ were achieved, similar to literature results for IE-NCM85,[29] but much lower than expected from a Ni-rich NCM.[32] To increase the specific capacity, the residual sodium within the structure, which is connected to the particle size, needs to be eliminated from the CAM. This can likely be achieved by lowering the particle size and reducing the sodium diffusion path lengths, as shown recently for size-tailored IE-LNO.[28]

2.2. Full Ion Exchange by Reducing Grain Size

The particle size of layered oxide CAMs can be reduced by the addition of surface segregating species, such as ammonium paratungstate.[28,33,34] Here, 2 mol% was added to prevent the growth/sintering of Na-NCM grains. The tungsten-doped sample (Na-NCM90-W) also consists of two phases with space groups $C2/m$ and $R\bar{3}m$ in a ratio of 20:80 by weight (see Rietveld refinement results in Table S1, Supporting Information), thus being less Jahn-Teller distorted than Na-NCM90. This points toward the introduction of tungsten into the bulk structure, leading to an overall larger fraction of the hexagonal phase. After ion exchange, we find 0.52 mol% tungsten relative to the sum of the other transition metals by inductively coupled plasma-optical emission spectroscopy (ICP-OES), as shown in **Table 2**. From this result, it can be concluded that the majority of tungsten segregates on the particle surface and is removed during the ion-exchange process.

Structural analysis of IE-NCM90-W revealed the presence of a single phase with an $R\bar{3}m$ space group; the Rietveld refinement results are given in **Table 3**. The parameters indicate good layering with a slightly larger unit-cell volume than reported in the literature,[2] which could be due to the residual sodium. Indeed, Rietveld refinement suggests 2.4% $Na_{Li}^{\times}$ defects, while the sodium content determined by ICP-OES is only 1.2 mol% (see Table 2). This is in agreement with previously reported data on tungsten-based size tailoring, indicating apparently increased electron density in the lithium slab, an effect likely caused by rock salt-type surface layer formation due to tungsten doping.[28] Overall, these results are indicative of a phase-pure material, as opposed to that obtained after ion exchange of the much larger Na-NCM90 particles.

2.3. Nickel Concentration Series – Microstructural Analysis

A series of IE-NCMs with nickel contents ranging from 88 to 100 mol% was synthesized by means of tungsten-based size tailoring. Hereafter, the samples are referred to as IE-LNO-W, IE-NCM95-W, IE-NCM90-W, and IE-NCM88-W for 100, 95, 90, and 88 mol% nickel content, respectively. The materials were probed using PXRD and ICP-OES, and the corresponding results are shown in Tables 2 and 3. All materials crystallize in the $R\bar{3}m$ space group and are obtained in single-phase form. They exhibit similar lattice parameters and unit-cell volume (with some minor increase with decreasing nickel content). IE-LNO-W also follows this trend, but the c lattice parameter is smaller, with ≈14.18 Å compared to ≈14.20 Å for the IE-NCM-W materials. This could be related to the relatively low residual sodium content, providing less pillaring to uphold the increased interlayer spacing from the parent NNO phase. However, upon closer examination of the diffraction pattern collected from IE-LNO-W (see Figure S2, Supporting Information), peak splitting (e.g., ≈20° 2θ) is observed, which may be indicative of symmetry reduction due to monoclinic distortion. Indeed, refining this material in the monoclinic space group $P2_1/c$ results in a better fit to the data. The corresponding results are given in Tables 3 and S3 (Supporting Information). In this analysis, the unit-cell volume of IE-LNO-W seems somewhat enlarged, potentially due to Jahn-Teller distortion. By ICP-OES, we find 1.2 mol% sodium in IE-LNO-W and 1.2–1.9 mol% in the IE-NCM-W materials, indicating that Rietveld refinement systematically overestimates the residual sodium content. The lithium content is ≈93 mol% for all samples, suggesting some lithium loss during the ion-exchange procedure, most likely upon water washing, which is known to have a more deleterious effect with increasing nickel content. Chemical oxidation of the samples during ion exchange could be a reason too. However, this would be evident from nuclear magnetic resonance (NMR) spectroscopy experiments and has not been observed previously.[27] Lastly, some of the lithium loss may also be due to the formation of rock salt-type surface impurities upon tungsten addition.[28]

To gain insight into the elemental distribution in the size-tailored materials, IE-NCM88-W was examined by TEM. The results obtained are shown in **Figure 3**. The imaging data indeed reveal a polycrystalline morphology, with the secondary particles appearing less dense in the center (see Figure 3a). As can be seen from the higher-magnification HAADF images in Figure 3b,c, the grain (primary particle) size is on the order of 50–400 nm. Regarding elemental distribution (see Figure 3e–h), the altered pre-annealing atmosphere seems effective in mitigating manganese segregation near the primary particle surface. Nevertheless, regions of higher concentration are still visible. The presence of small amounts of sodium is also apparent, but not in the form of domains as observed for IE-NCM90. Lithium localization was achieved by electron energy loss spectroscopy (EELS) mapping (see Figure 3d), suggesting uniform distribution throughout the primary grains. However, the specific grain examined was located in the center of the secondary particle and thus may not have been exposed to water during the washing step after ion exchange. High-resolution TEM analysis (see Figure 3i–l) further indicates that the surfaces oriented parallel to the stacking direction are more disordered (≈1–5 nm thick layers) than those oriented parallel to the layering direction. Similar features are observed for other primary particles of the same material (see Figure S3, Supporting Information). This may suggest preferential migration of tungsten depending on the crystal facet, similar to observations made for ion-exchanged LNO when

Table 3. Structural parameters determined by Rietveld refinement for IE-LNO-W, IE-NCM95-W, IE-NCM90-W, and IE-NCM88-W. Parameters marked with an asterisk indicate the equivalent values in a hexagonal space group (see Table S2, Supporting Information, for details).

Sample	Phase	wt.%	R_{wp} [%]	R_{Bragg} [%]	a [Å]	c [Å]	V [Å^3]	$Na_{Li}^{\times}$ [%]
IE-LNO-W	$R\bar{3}m$	100	16.3	3.7	2.8775(12)	14.1768(156)	101.679(150)	3.8(22)
	$P2_1/c$	100	17.4	2.9	a^* = 2.8936(15)	c^* = 14.3037(16)	V^* = 103.718(60)	0.5(2)
IE-NCM95-W	$R\bar{3}m$	100	20.3	4.2	2.8775(4)	14.2023(12)	101.836(45)	3.7(32)
IE-NCM90-W	$R\bar{3}m$	100	12.9	3.3	2.8778(3)	14.1992(25)	101.837(30)	2.4(26)
IE-NCM88-W	$R\bar{3}m$	100	11.7	2.1	2.8789(2)	14.2094(9)	102.055(20)	4.0(7)

tungsten is used to tailor the particle size (see Figure S3, Supporting Information). It was attempted to localize these tungsten impurities by EDS mapping, but unfortunately, the signal is too weak to allow for unambiguous identification (see Figure S4, Supporting Information). However, the observed amorphization could also be related to damage induced by the electron beam. Additionally, layer gliding is observed, which may be attributed to mechanical deformation during the ion-exchange reaction.

Overall, the TEM results provide evidence that size tailoring is effective in removing sodium from the lattice and corroborate the ICP-OES and PXRD data. Furthermore, they demonstrate that changing the pre-annealing atmosphere from oxygen to argon is beneficial for improving the distribution of transition-metal species. The location of tungsten could not be conclusively analyzed, but the formation of a disordered surface layer points toward preferential accumulation at the surfaces oriented parallel to the stacking direction.

2.4. NMR Spectroscopy

The samples were also probed by ^{7}Li magic-angle spinning (MAS) NMR spectroscopy (see **Figure 4**). Compared to the spectrum of large-sized IE-LNOs,[27] the size-tailored IE-LNO-W reveals several distinct lithium environments. The most pronounced peak centered at 702 ppm is relatively narrow, and no signal is detected beyond 800 ppm, evidencing its $Ni_{Li}^{\bullet}$-free nature.[27] Additional smaller and shoulder peaks are visible at 640, 665, 734, and 795 ppm. Also, clusters of peaks are observed at 487 and 511 ppm. Recently, the presence of twin and antiphase boundaries has been associated with peaks in

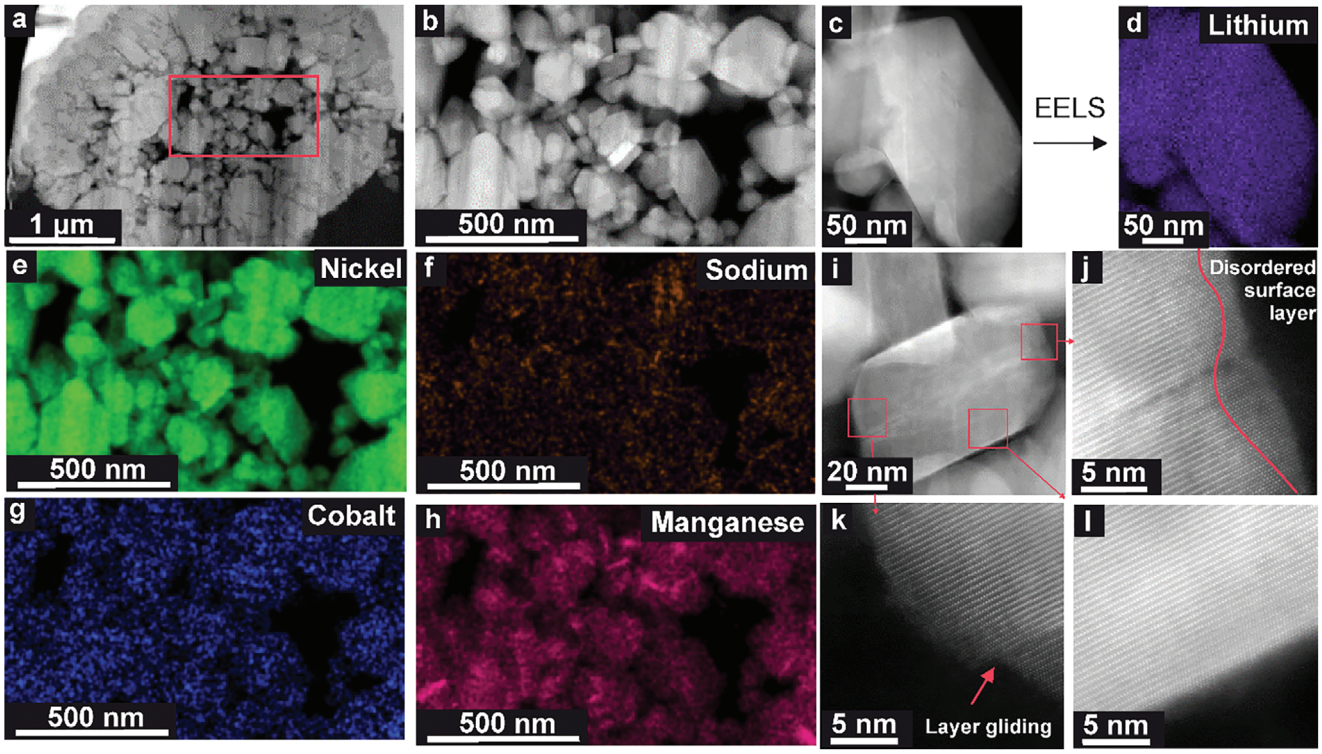

Figure 3. (S)TEM analysis of FIB-prepared IE-NCM88-W with the area probed by EDS indicated by a red rectangle in (a). b) Higher-magnification HAADF image of the region of interest. c) HAADF image of the region used for (d) EELS analysis of lithium distribution. e–h) EDS maps for nickel, sodium, cobalt, tungsten, and manganese. i) HAADF image of a single grain with the areas probed by high-resolution imaging (j–l) indicated by red rectangles.

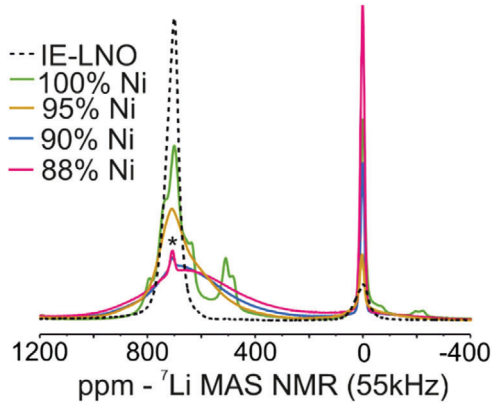

Figure 4. Normalized ^{7}Li MAS NMR spectra (55 kHz) of large-sized IE-LNO[27] and the IE-LNO/NCM-W samples. The spinning sideband of the 0 ppm peak is marked with an asterisk.

that region.[35] Specifically, the shifts that were calculated to be in the ranges of 542–690 ppm, 794–954 ppm, and 484–590 ppm for lithium atoms located away, close to, and at the antiphase boundary, respectively, agree well with the aforementioned additional peaks. Furthermore, the presence of W^{6+} may cause charge compensation effects in the transition-metal substructure, thus leading to Ni^{2+} formation. This would result in higher shifts, i.e., ppm values for the described lithium environments. Some of the signals could also originate from the disordered surface regions having high tungsten content or from tungsten substitution in the bulk structure. Nevertheless, the main signal exhibits no shift to higher ppm values, which would otherwise be characteristic of the presence of $Ni^{\bullet}_{Li}$ defects.[27,35,36]

With decreasing nickel content, the main peak becomes broadened, as expected due to the multiple Ni/Mn/Co environments (resulting in Ni^{2+} formation) around lithium. While for IE-NCM95-W, the pattern of the undoped material is still somewhat visible, it vanishes completely for the other two samples due to extreme peak broadening. Therefore, not much information can be gathered for both IE-NCM90-W and IE-NCM88-W by NMR spectroscopy other than the fact that the main peak position is shifting to lower ppm values for IE-NCM88-W (to ≈665 ppm). Additionally, the spinning sideband of lithium residuals in a diamagnetic environment at 710 ppm makes analysis more challenging.

Taken together, the data confirm the lack of $Ni^{\bullet}_{Li}$ defects for samples prepared by ion-exchange synthesis. A contribution to peak broadening may be structural disorder, i.e., variations in bond length/angle, induced by the additional transition metals (Co/Mn) or the grain size.[37] However, the materials also contain lithium in considerable amounts in defective sites, which are likely introduced by tungsten addition. A signal is observed at 0 ppm, which can be linked to diamagnetic lithium salts present on the particle surface.[38] Interestingly, for the IE-NCM-W CAMs, this signal increases with increasing degree of substitution. As shown in **Figure 5e**, the particle size decreases and the specific surface area increases in the same direction. Consequently, variations in surface area could account for the increase in lithium residuals (originating from leaching upon water exposure during washing).

2.5. Morphology

The morphology of the ion-exchanged materials was investigated by scanning electron microscopy (SEM, see Figure 5a-d). Relatively small primary particles in the size range of d_{50} = 132–226 nm are observed for all samples (see Figure 5e). This finding corroborates the successful mitigation of sintering due to tungsten addition, as already described for IE-NCM88-W in Figure 3. The grain size decreases slightly with decreasing nickel content, which is likely related to reduced growth caused by the presence of cobalt and manganese. Regardless, the primary particle sizes are representative of those typically achieved in Ni-rich CAMs prepared by solid-state synthesis.[20,39] The degree of agglomeration, or in other words, the retention of the original polycrystalline morphology, differs between the samples. This seems to point toward higher mechanical stability of the secondary particle structure with lower nickel content, although IE-NCM-90-W does not perfectly fit this trend. Partial deagglomeration is expected to correlate with the extent of surface degradation due to side reactions in the aqueous washing step, meaning that the primary particles undergo lithium-to-proton exchange at the surface. Furthermore, one could argue that lithium diffusion in a polycrystalline particle would add to kinetic limitations and thus to capacity loss. While we cannot fully exclude this possibility, such an effect would certainly lead to stronger differences in the diffusion-based capacity loss between the samples, which we do not observe (as described below). Therefore, the primary particle size is the key parameter, which does not differ much among the described materials and allows for a reasonable comparison of the electrochemical performance.

2.6. Electrochemistry

The materials were electrochemically tested by galvanostatic cycling in LIB half-cells at a C/10 rate in the potential window of 3.0-4.3 V versus Li^{+}/Li. As can be seen from the first-cycle voltage profiles in **Figure 6a–d**, the specific charge capacities increase with decreasing nickel content, from q_{ch} = 200 mAh g_{CAM}^{-1} for IE-LNO-W to q_{ch} = 235 mAh g_{CAM}^{-1} for IE-NCM88-W. Similarly, the specific discharge capacities increase from q_{dis} = 173 mAh g_{CAM}^{-1} (IE-LNO-W) to 202 mAh g_{CAM}^{-1} (IE-NCM95-W), 183 mAh g_{CAM}^{-1} (IE-NCM90-W), and 199 mAh g_{CAM}^{-1} (IE-NCM88-W). Clearly, transition-metal substitution helps to increase the extractable charge. This may be due to the more reactive surface of LNO compared to the Ni-rich NCMs, causing more severe detrimental side reactions.[40] During water washing, LNO is known to undergo lithium-to-proton exchange, leading to some degradation of the material.[41] As mentioned above, ICP-OES analysis indicates a lack of lithium, however, independent of the nickel content. Since the extent of lithium deficiency is similar for the different CAMs, it is likely not responsible for the lower specific capacity of IE-LNO-W. Nevertheless, the stability of the partially protonated surface is expected to differ among the samples and is believed to cause capacity loss, especially in the case of IE-LNO-W. The increase in charge capacity with decreasing nickel content is somewhat unexpected; the opposite trend is usually observed for CAMs produced by solid-state synthesis. However, this is only related to the cutoff potential, i.e., to what

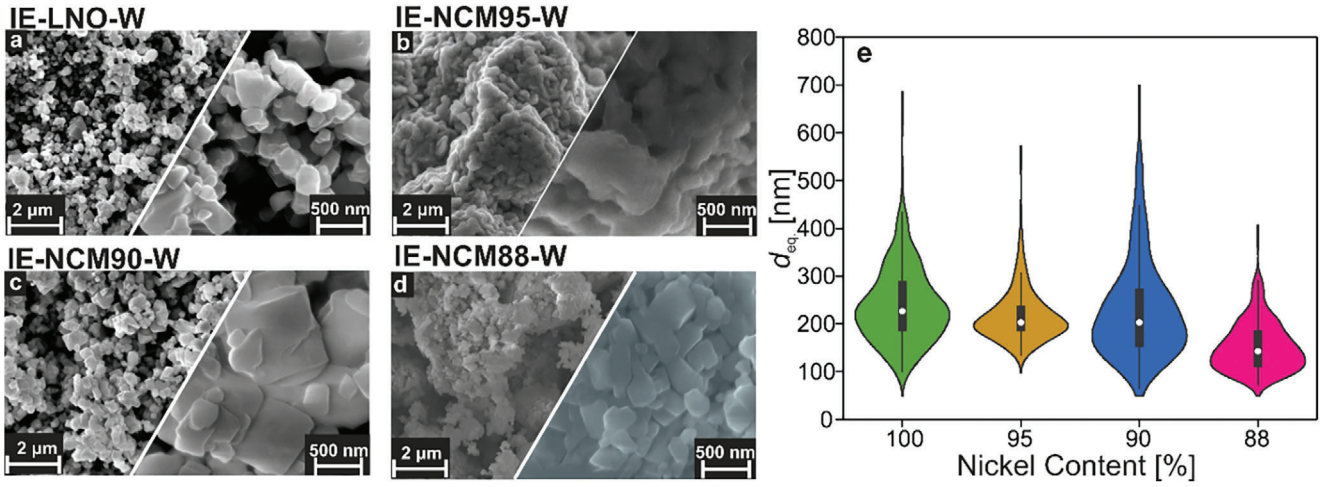

Figure 5. SEM images of a) IE-LNO-W, b) IE-NCM95-W, c) IE-NCM90-W, and d) IE-NCM88. e) Corresponding size analysis (see Supporting Information for details).

extent the material is delithiated at a given charge cutoff.[5] As can be seen from Figure 6, all materials experience the characteristic phase transitions in Ni-rich NCMs, including the H2-H3 transition, with the latter occurring well below the cutoff potential due to the absence of $Ni^{\bullet}_{Li}$ defects (see Figure S5, Supporting Information, for details). Considering that the materials employed in this work undergo the same phase transitions, the SOC of the respective cells should be comparable (depending on the fraction of electrochemically active material and the degree of degradation).

The first-cycle capacity loss does not show a linear relation with nickel content. Interestingly, IE-NCM95-W performs best, with only 24 mAh g_{CAM}^{-1} or 10.6% capacity loss, while the other materials exhibit losses exceeding 14%. The first-cycle loss was separated into kinetic hindrance and degradation at high potentials by aligning the charge and discharge curves in the region corresponding to $Li_{2/5}Ni_xCo_yMn_zO_2$, as shown in **Figure 7a-c**.[42] This phase is chosen specifically as it is most clearly recognizable as a single-phase region in all of the first-cycle voltage profiles, while being in a range that is likely more stable than the high-voltage H2 and H3 phases. The results from this analysis are presented in Figure 7d. With decreasing nickel content, an increase in capacity loss due to kinetic hindrance (KH) is observed, from 2.5% in IE-LNO to 10.3% in IE-NCM88-W. This could be attributed to sluggish lithium diffusion in the bulk or degradation of the material's surface. With regard to surface stability, the opposite trend would be expected from the available literature, as Ni-rich NCMs tend to release less lattice oxygen than LNO, suggesting that surfaces and interfaces are more stable/robust.[40] This, in turn, means that the degraded surface

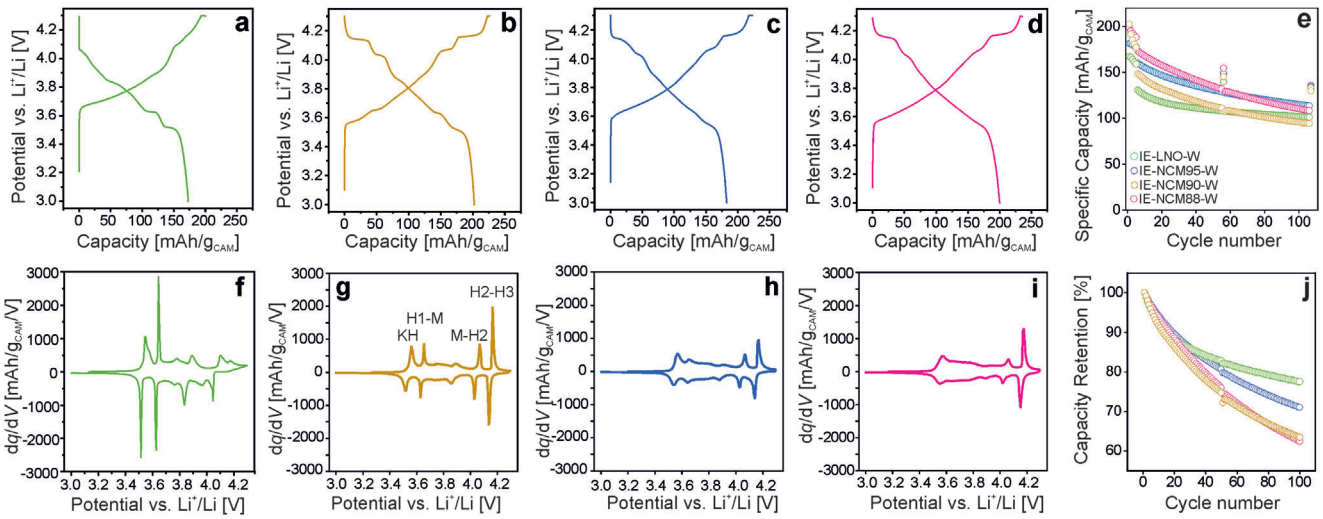

Figure 6. First-cycle voltage profiles and second-cycle differential capacity curves for a,f) IE-LNO-W, b,g) IE-NCM95-W, c,h) IE-NCM90-W, and d,i) IE-NCM88-W. e) Long-term cycling performance with 5 cycles at C/10, 50 cycles at 1C charge and C/2 discharge, 1 cycle at C/10, and 50 cycles at 1C charge and C/2 discharge in the potential window of 3.0–4.3 V versus Li^+/Li. j) Capacity retention relative to the 6th cycle at 1C charge and C/2 discharge. Note that the 56th cycle at C/10 is omitted for clarity.

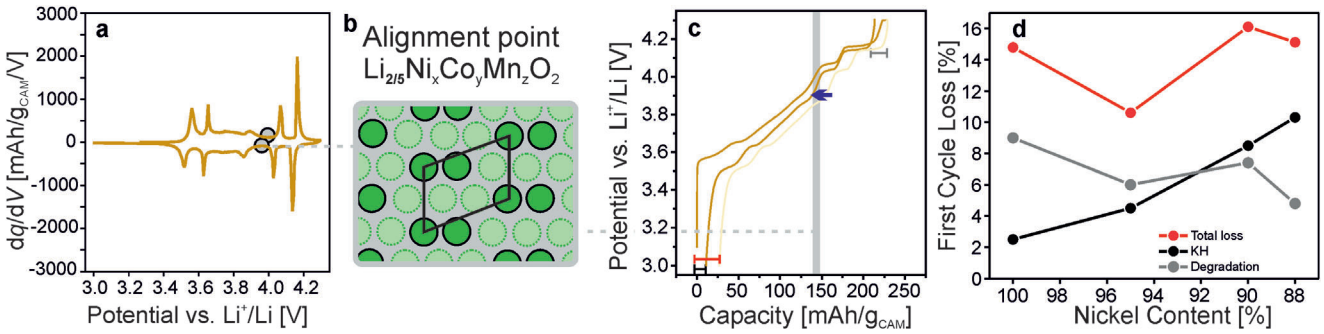

Figure 7. a) Second-cycle differential capacity curve of IE-NCM95-W with an indication of the alignment points. b) Schematic representation of lithium/vacancy ordering in the phase corresponding to the alignment points. c) Aligned first-cycle charge/discharge curves. d) Results from first-cycle capacity loss analysis. KH refers to kinetic hindrance loss.

of LNO would add more to losses associated with lithium diffusion than that of a Ni-rich CAM. However, as indicated by (S)TEM of IE-NCM-88 in Figure 3, which is substituted most, manganese does not segregate at the surface if the pre-annealing step is performed in an inert atmosphere. The stability at high SOC follows the opposite trend. With decreasing nickel content, the reversibility in the high-voltage range increases. This observation agrees well with the increased surface stability of NCMs.[40] As for polarization, no differences that would be indicative of facilitated lithium diffusion at low potentials are observed with decreasing nickel content. In fact, polarization is more pronounced in the case of IE-LNO.

2.7. Trends in Stability, Diffusion, and Jahn-Teller Distortion

To gain more insight into the impact of cobalt and manganese substitution on lithium diffusion, the differential capacity (dq/dV) curves shown in Figure 6f–i were compared. The peaks seen for IE-LNO-W have previously been assigned to the same transitions occurring in LNO prepared by conventional solid-state synthesis,[27] and similar peaks are apparent for the IE-NCM-W samples. In short, when going from low to high potential, the observed peaks correspond to the so-called "kinetic hindrance", H1-M, M-H2, and H2-H3 transitions (see Figure 6g for peak assignments). In the case of IE-LNO-W, the KH and H1-M transitions are characterized by the presence of distinct peaks. However, the M-H2 and H2-H3 transitions appear broadened and shifted compared to IE-LNO. This may be caused by hysteresis at high SOC, which has been hypothesized to be due to sluggish (de)lithiation of a surface rock salt-type phase.[43] The formation of such a phase could be facilitated by lithium-to-proton exchange, a process known to occur when subjecting LNO to water washing (and subsequent thermal decomposition of the resulting NiO(OH) phase during drying of the electrode).[41] An alternative explanation for the increased polarization is provided by the theoretical work of Xiao et al. They hypothesize that lithium diffusion from the H2 phase into the H3 phase is rate-limiting during charging, causing a nucleation barrier for the formation of (collapsed) NiO_2.[44] Specifically, the free surface is assumed to facilitate phase transitions by affecting the Li-Li interactions. In a similar fashion, substitutional defects in the transition-metal site may also facilitate the H2-H3 transition, as indicated by the decrease in polarization. This observation falls in line with the emergence of solid-solution behavior (see below).

As evident from the data in Figure 6, the KH and H1-M peaks decrease with decreasing nickel content. This indicates slower lithium diffusion at the end of discharge, as well as a reduction in the degree of monoclinic distortion. The latter can be explained by a weaker interplay between lithium/vacancy ordering and Jahn-Teller activity of Ni^{3+} ions.[42,45] Also, the lower nickel content and changes in oxidation state caused by Mn^{4+} residing on the transition-metal site[46] contribute toward mitigating Jahn-Teller distortion. At high SOC, the peaks related to the M-H2 and H2-H3 transitions become more pronounced for IE-NCM95-W, and they are less shifted compared to those of IE-LNO-W. However, a further increase in nickel content seems to broaden and diminish the H2-H3 peak. The M-H2 peak, on the other hand, clearly decreases with decreasing nickel content, similar to the H1-M peak, which is due to the loss of Jahn-Teller-active species and disruption of lithium/vacancy ordering, as explained above.

Regarding cycling stability (see Figure 6e,j), the polycrystalline samples (IE-NCM95-W and IE-NCM88-W) deliver the highest specific capacities, but also exhibit the most severe fading, which is likely caused by intergranular cracking. By contrast, the more isolated particles of IE-LNO-W and IE-NCM90-W deliver lower specific capacities, but cells using these materials show better capacity retention. No clear correlation between capacity or capacity retention and degree of substitution is observed since the effects of processing likely outweigh the fine differences between the stoichiometries tested.

Overall, the results achieved by reducing the nickel content seem to be threefold. First, stabilization of the high-voltage regime is apparent, similar to conventionally synthesized NCMs.[40] Similarly, in the literature, manganese incorporation has been reported to negatively affect lithium diffusion, while substitution with cobalt has beneficial effects on mobility.[21] However, the authors commented on the possibility of variations in cation intermixing being the cause of differences in diffusivity. In the present work, the CAMs employed do not contain $Ni^{\bullet}_{Li}$ defects, thus ruling out the latter explanation. Another factor that can affect the capacity in the KH region is the primary particle (grain) size. The expected trend would be a decrease in capacity loss with decreasing size. However, the opposite is observed here. Therefore, a previously unreported mechanism seems to affect lithium diffusion. Our hypothesis for this is the pinning

of lithium vacancies, which would slow down diffusion and has been shown to occur in the vicinity of $Ni_{Li}^{\bullet}$ defects.[47] Lastly, the data indicate changes to the degree of monoclinic distortion, which may have several reasons. Loss of Jahn-Teller-active species upon substituting nickel with cobalt and manganese and reduction of the average nickel oxidation state due to manganese incorporation are expected. Another reason could be the disruption of lithium/vacancy ordering due to the pinning of lithium vacancies induced by the altered composition, as already mentioned with regard to the trends seen in lithium diffusion.

2.8. Operando XRD

Several factors were shown to contribute to the Coulomb efficiency in the first cycle. In short, a combination of kinetic hindrance and material degradation yields the overall capacity loss. For kinetic hindrance, a clear inverse correlation with nickel content is observed (the higher the nickel content, the lower the KH loss), while the loss related to high-voltage degradation follows the opposite trend. For the CAMs studied here, IE-NCM95-W is found to exhibit the lowest first-cycle capacity loss.

To compare the structural evolution of IE-LNO-W, IE-NCM95-W, and IE-NCM88-W during cycling, *operando* XRD measurements were conducted on LIB half-cells. The data acquired and the corresponding refinement results (see Experimental section and Figures S6 and S7, Supporting Information, for details) are shown in **Figure 8**. The cells were cycled in the potential window of 2.9–4.5 V versus Li^+/Li at C/20, and the PXRD patterns collected during discharge were analyzed by sequential Le Bail refinement. Due to thermal noise problems of the detector, some of the patterns could not be used for reliable refinement. As can be seen from the contour plot in Figure 8a, IE-LNO-W shows clearly two-phase behavior in the high-voltage regime. The latter causes minor variations in the lattice parameter *a*, with −0.5% difference between H2 and H3, while the lattice parameter *c* and the unit-cell volume undergo relative changes of −8.4% and −9.1%, respectively. For IE-NCM95-W, two-phase behavior in the H2-H3 region is still apparent, however, decreasing the nickel content further leads to solid-solution behavior (see Figure 8b,c). The volume change during the phase transition decreases to −5.2% for IE-NCM95-W. Also, the overall volume change from discharged to charged state decreases from −12.7% for IE-LNO-W to −9.6% for IE-NCM95-W (−9.3% for IE-NCM88-W). This result indicates that increasing the nickel content from 88% or 95% to 100% has a profound effect on the volume variation during cycling and may help explain why CAMs with a very high nickel content typically experience stronger fading and oxygen evolution,[40] even though the absolute volume change of NCMs is not much affected by the nickel content.[2] Especially the abrupt volume variation and the co-existence of two, increasingly different phases, as opposed to solid-solution behavior, are believed to negatively affect stability. Furthermore, the results indicate a stabilizing effect of $Ni_{Li}^{\bullet}$ defects on the high-voltage H2-H3 transition. This is consistent with the calculated linear relationship between the potential of the phase transition and the $Ni_{Li}^{\bullet}$ fraction.[42] With 95% nickel content, two-phase behavior is observed (i.e., the presence of two distinct layered phases), while literature data indicate a smoother transition for NCM95.[48] Hence, the results stress the importance of intrinsic $Ni_{Li}^{\bullet}$ defects for achieving long-term stability of state-of-the-art Ni-rich NCM and LNO CAMs. Accordingly, $Ni_{Li}^{\bullet}$ defects should be thought of as a functional modification to the CAM, which can have beneficial and/or detrimental effects on cycling performance.

With regard to the monoclinic distortion region, ranging from 3.6 to 3.9 V, distinct peak separation is observed for IE-LNO-W, while IE-NCM95-W exhibits diffuse peaks and IE-NCM88-W reveals single-phase behavior (in the range of 3.45–3.90 V). Because monoclinic distortion is caused by the coupling of lithium/vacancy ordering and Jahn-Teller-active Ni^{3+}, it is expected that cobalt and/or manganese incorporation reduces the degree of distortion by altering the overall nickel content, the nickel oxidation state (only Mn^{4+}), and the lithium distribution. Nevertheless, we find clear signs of monoclinic distortion in the 95% nickel sample. Note that this may be more pronounced due to the lack of $Ni_{Li}^{\bullet}$ defects, which disturb the lithium/vacancy ordering and introduce $Ni_{Ni}^{\prime}$ defects (get oxidized quickly upon charging though).[18,42,47] The monoclinic distortion in IE-NCM95-W is smaller than that of IE-LNO-W, which is evident from the difference between the a^* and b lattice parameters and β (see Figure S8, Supporting Information).

Taken together, the *operando* XRD analysis reveals the presence of two-phase regions with relatively large changes in unit-cell volume at high SOC, as well as a distinct monoclinic distortion for IE-LNO. Upon cobalt and manganese substitution, the phase transitions become less apparent. However, in comparison to results available in the literature,[48] less solid-solution behavior is observed. The absence of $Ni_{Li}^{\bullet}$ defects seems to intensify the differences between crystallographic phases and lead to a more biphasic behavior. Intrinsic point defects likely stabilize LNO and state-of-the-art Ni-rich CAMs against degradation, an effect that should be considered when assessing the cycling performance of such materials.

2.9. Vacancy-Pinning Hypothesis

In recent years, it has been shown that $Ni_{Li}^{\bullet}$ defects can slow down the kinetics of LNO both by diminishing the number of ionic charge carriers and increasing the length of diffusion paths.[18,42,47] The positive charge of excess nickel in the lithium layer, along with the accompanying local chemo-mechanical strain, creates an attractive potential for lithium vacancies that also considerably lowers the migration barrier for a lithium vacancy to approach the defect, effectively making $Ni_{Li}^{\bullet}$ defects sinks for lithium vacancies. Following the same line of thought, we conducted a similar study to investigate the thermodynamics of lithium-vacancy formation in the vicinity of isolated cobalt and manganese dopants in the nickel layer, corresponding to a concentration of 1.6% per layer or 0.8% per cell. We calculated the vacancy-stabilization energy for individual lithium vacancies with respect to the energy of the farthest vacancy from the dopant.

Figure 9 illustrates the top view of the Ni layer with the dopant, where lithium sites in the Li layer are represented as small green points. Superimposed on this view are color maps that depict the vacancy-stabilization energy (see Figure 9a,b) and the volumetric strain experienced by each lithium-ion (see Figure 9d,e) resulting from the substitution of nickel with cobalt and

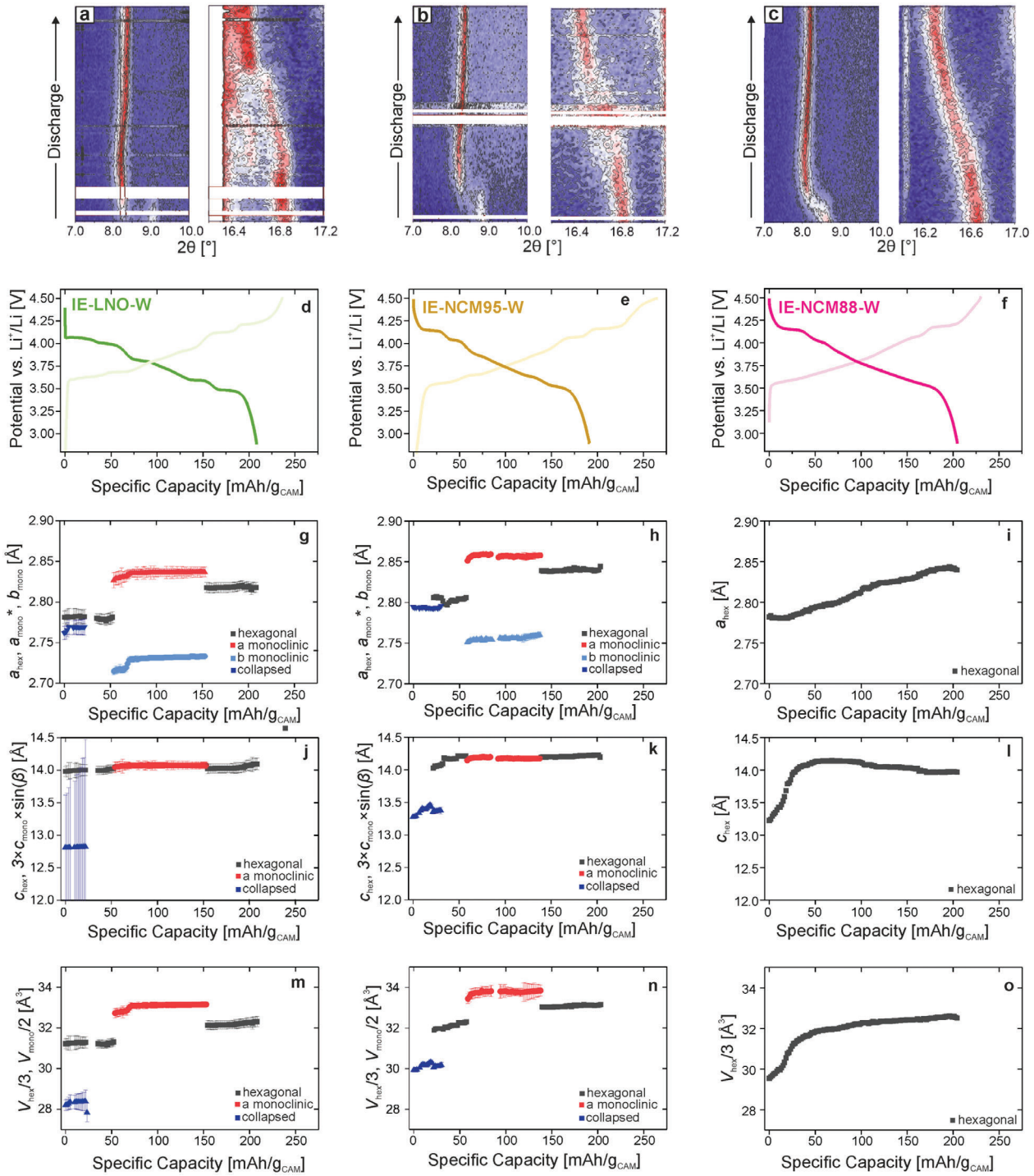

Figure 8. Contour plots of *operando* XRD data collected from a) IE-LNO-W, b) IE-NCM95-W, and c) IE-NCM88-W during discharge from 4.5 to 2.9 V versus Li^+/Li at a rate of C/20. d–f) Corresponding voltage profiles and results from sequential Le Bail analysis for g,j,m) IE-LNO-W, h,k,n) IE-NCM95-W, and i,l,o) IE-NCM88-W.

manganese. The effect of $Ni^{\bullet}_{Li}$ defects is shown in Figure 9c,f for comparison. Upon initial observation, it becomes apparent that the vacancy-stabilization energies are predominantly negative for both cobalt and manganese, suggesting a vacancy-pinning effect akin to $Ni^{\bullet}_{Li}$. This effect is more pronounced in the proximity of manganese than cobalt, evident from both the magnitude of stabilization (energy scale) and the spatial extent of the trapping pattern. The weaker influence of cobalt is consistent with findings by Li et al.[49] The stabilization of specific lithium sites can be partially explained by the volumetric strain

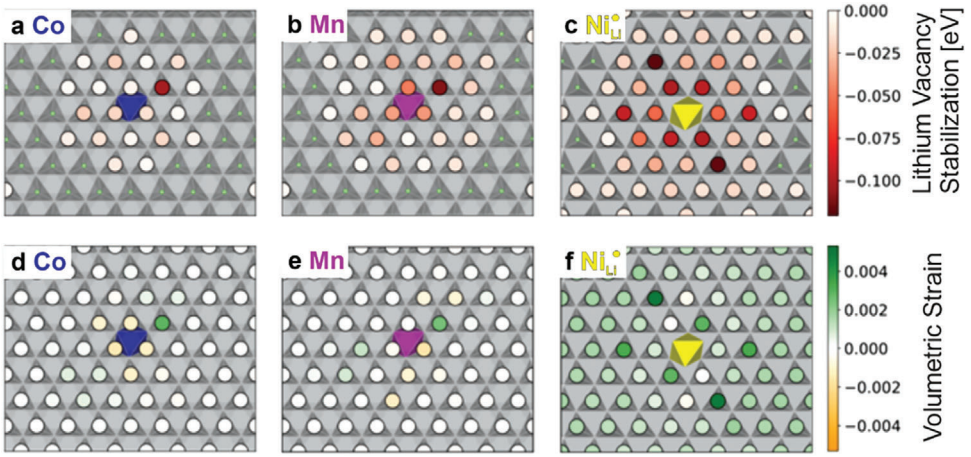

Figure 9. a,b,c) Lithium-vacancy stabilization energies and d,e,f) volumetric strains in the presence of dilute amounts of cobalt (blue) and manganese substitutional dopants (purple) as well as $Ni_{Li}^{\bullet}$ point defects (yellow). The underlying Ni—O lattice is depicted as gray polyhedra. Lithium sites in the Li layer are indicated by small green points, with circular markers representing explicitly calculated points. The Li layer underneath the Ni—O layer shows similar patterns, with the transition metal acting as an inversion center.

that occurs when cobalt or manganese substitutes nickel. Notably, the lithium site connected to the dopant through the previously elongated Jahn-Teller distorted Ni—O bond experiences the highest strain. It is evident that substituting Ni^{3+} with a non-Jahn-Teller-active ion inevitably introduces non-negligible local strain. It is important to note that both strain and stabilization energy exhibit centrosymmetry relative to the position of the dopant. This indicates that similar pinning effects will also be observed in the Li layer below the dopant. Therefore, the number of affected lithium vacancies is twice what is shown in Figure 9. Delmas et al. linked the pinning of six lithium ions to each $Ni_{Li}^{\bullet}$ defect,[50] and we have explicitly computed that this is a realistic estimate.[47] Based on visual inspection, manganese and especially cobalt seem to be less effective vacancy traps than $Ni_{Li}^{\bullet}$. In the past, we have calculated the effects of vacancy pinning on the smoothing of voltage profiles and the suppression of phase transitions and compared them to experimental results,[42] concluding that the major effect of substitutional strategies is the disruption of lithium/vacancy orderings, which in turn results in the establishment of solid solutions and the progressive elimination of phase transitions. However, both dopants are present simultaneously in NCMs and in greater concentrations, meaning that their strain fields are bound to overlap and could lead to unexpected trapping patterns in these configurations. To gain a qualitative understanding, we conducted the strain analysis on a relaxed NCM88 model ($Li_{128}Ni_{112}Co_8Mn_8O_{256}$) with uniformly distributed cobalt and manganese. Although even the distribution of dopants is reasonable, it may not be realistic if the substituents have a tendency to cluster or segregate. The strain analysis is presented in **Figure S9** (Supporting Information), clearly illustrating overlapping effects in close proximity to the substituents, as well as in the regions between them.

3. Conclusion

LNO and the related Ni-rich NCMs intrinsically contain $Ni_{Li}^{\bullet}$ substitutional defects, which are generally believed to be detrimental by impeding lithium diffusion. Herein, we successfully studied a series of Ni-rich cathodes synthesized by sodium-to-lithium ion exchange. In contrast to state-of-the-art positive electrode materials, the ion-exchanged samples are devoid of $Ni_{Li}^{\bullet}$ defects and thus serve as an ideal platform to examine the intrinsic role of transition-metal site dopants, without intermingling effects induced by substitution and point defects. We find that the nickel content affects the first-cycle specific capacity, with higher concentrations allowing for faster diffusion, particularly at the end of discharge. We hypothesize a mechanism involving lithium-vacancy pinning to be responsible for this observation and confirm the results by DFT calculations. However, lower nickel contents are associated with increased stability at high SOC. The latter was studied in some more detail by *operando* XRD, indicating more severe phase transitions during cycling with approaching 100 mol% nickel content. Furthermore, we demonstrate that point defects help to mitigate the negative effects of electrode breathing (volume variation) and suggest that the $Ni_{Li}^{\bullet}$ fraction should be considered more carefully when studying Ni-rich NCM and NCA cathode materials, since the stabilizing effects of cobalt, manganese, and $Ni_{Li}^{\bullet}$ emerge simultaneously.

4. Experimental Section

Synthesis of NNO and Na-NCMs: $Ni(OH)_2$ or co-precipitated NCM hydroxide pCAM particles (BASF SE; d_{50} = 4.0 µm with 100:0:0, 95:4:1, 90:5:5, and 88:5:7 Ni:Co:Mn molar ratios) were mixed with 1.1 eq. NaOH (Sigma-Aldrich) and, if stated, with 0.02 eq. ammonium paratungstate (Sigma-Aldrich) using a laboratory grade blender. The powder mixtures were first pre-annealed at 300 °C for 10 h in argon (unless stated otherwise in the main text) with two atmosphere exchanges per hour. Subsequently, the samples were mixed again under an inert atmosphere, followed by calcination at 700 °C for 12 h in oxygen with two atmosphere exchanges per hour and 3 K min^{-1} heating and cooling rates.

Ion-Exchange Procedure: Sodium-to-lithium ion exchange was accomplished by mixing NNO or Na-NCMs with $LiNO_3$ (1:1 by weight) in a mortar and pestle. The powder mixtures were then filled into alumina crucibles and heated at 300 °C for 6 h, without control over the atmosphere. After cooling to room temperature, the samples were washed twice with 1:10 by weight of CAM to 0.025 M LiOH solution in DI water for a total of 30 min.

Residual water was removed by washing with ethanol and acetone, followed by drying under vacuum at 70 °C. Prior to electrochemical testing, the samples were sieved using a 32 µm stainless-steel mesh.

Electrochemical Testing: The CAM particles were first mixed with polyvinylidene difluoride binder (PVDF; Solef 5130, Solvay) and Super C65 carbon additive (TIMCAL Ltd.) in a ratio of 94:3:3 by weight and then cast onto 0.03 mm thick aluminum foil using a stainless-steel blade with a slit thickness of 140 and 200 µm for electrochemical and *operando* XRD testing, respectively, using an Erichsen Coatmaster 510 applicator (resulting in areal loadings of approx. 10 and 14 mg cm^{-2}, respectively). The as-prepared electrode tapes were dried in a vacuum at 120 °C, calendared at 14 N mm^{-1} (Sumet Messtechnik), and cut into circular 13 mm diameter discs. Coin cells were assembled using a glass fiber GF/D separator, LP57 electrolyte (1 M $LiPF_6$ in 3:7 by weight of ethylene carbonate and ethyl methyl carbonate), and a lithium-metal anode in an argon glovebox.

SEM: Sample imaging/mapping was carried out using a LEO-1530 microscope (Carl Zeiss AG).

FIB Cutting: Electron-transparent samples were produced by the lift-out technique using an FEI Strata 400 S dual-beam system. Sample damage and amorphization from the gallium-ion beam were minimized by stepwise reduction of the acceleration voltage from 30 to 2 keV during the final thinning of the lamellae. Specimen preparation was immediately followed by a TEM investigation.

(S)TEM: Measurements were carried out on a probe aberration-corrected Thermo Fisher Scientific Themis Z microscope at 300 kV. EDS maps were acquired using a Super-X EDX detector.

ICP-OES: A Thermo Fisher Scientific ICAP 7600 DUO was used for ICP-OES analysis. Specifically, the samples were dissolved in an acid digester in a graphite furnace. Mass fractions were obtained from three independent measurements. About 10 mg of material was dissolved in hydrochloric acid and nitric acid at 353 K for 4 h. The digested samples were diluted for analysis. The range of calibration solutions did not exceed a decade. Two or three wavelengths of the elements were used for quantitative analysis.

PXRD: Patterns were collected on a STADI P (STOE) diffractometer in Debye-Scherrer geometry using monochromatic Mo-$K_{\alpha 1}$ radiation (λ = 0.7093 Å, 50 kV, 40 mA) and a Mythen 1K detector (DECTRIS AG). The datasets were analyzed using the TOPAS-Academic v7 software. Le Bail fitting was done first, in which background correction was applied by a set of Chebyshev polynomials, and lattice parameters, zero-shift, axial divergence, and crystallite size were extracted as Gaussian and Lorentzian contributions. During Rietveld refinement, the parameters from Le Bail fitting were first fixed, and the oxygen coordinates z_O (LNO) and z_{O_1} and z_{O_2} (NNO), site occupancies, and Debye-Waller factors were refined while applying an absorption correction. Eventually, all parameters were refined in parallel until convergence was achieved. The confidence intervals were three times the estimated standard deviations as obtained from TOPAS-Academic v7 software.

Solid-State NMR Spectroscopy: ^{7}Li MAS NMR spectroscopy measurements were carried out on a Bruker AVANCE NEO instrument at a magnetic field of 4.7 T, corresponding to a resonance frequency of 77.8 MHz. Spinning was performed in 1.3 mm rotors at 55 kHz. NMR spectra were acquired with a Hahn echo pulse sequence, a $\pi/2$ pulse length of 0.85 µs, and a recycle delay of 1 s. The ^{7}Li chemical shifts were referenced to a 1 M LiCl solution at 0 ppm.

Operando XRD: The positive/negative caps and spacers of the coin-cell casing were modified by electro-erosion to have a hole of 5 mm diameter in the middle and then sealed with Kapton foil of 6 mm diameter and 160 µm thickness. The cells were cycled at a rate of C/20 using a Gamry Interface 1000 potentiostat, while patterns were collected simultaneously using an STOE Stadi-P diffractometer with a Mo anode. Data were acquired in the range $5° < 2\theta < 37°$ with a collection time of 10.3 min per pattern. Le Bail fitting was carried out sequentially on the diffraction data using the TOPAS-Academic v7 software. The zero offset was refined for each cell component individually, and the instrumental contribution to peak broadening was determined by measurement of a LaB_6 660b standard.

Theory: The Vienna Ab initio Simulation Package (VASP)[51,52] was used to perform spin-polarized DFT calculations with projector-augmented wave pseudopotentials[53,54] and the optB86b-VdW exchange-correlation functional[55] that has recently been used to model intercalation compounds.[36,42,56,57] Isolated cobalt and manganese dopants were inserted in a 2·8·4 supercell of the $P2_1/c$ cell of LNO, allowing for the proper Jahn-Teller distortion caused by Ni^{3+} ions.[58,59] Structural models have been fully relaxed by releasing all degrees of freedom (ionic positions, cell shape, and volume) with a cutoff energy of 600 eV and a *k*-point spacing of 0.5 $Å^{-1}$ until the forces were lower than 10^{-2} eV $Å^{-1}$. The convergence criterion for the electronic self-consistent cycles was set to 10^{-5} eV; the minimum number of electronic self-consistency steps was set to 6, which occasionally enforced tighter convergence. Atomic volumetric strains were calculated using OVITO.[60]

Supporting Information

Supporting Information is available from the Wiley Online Library or from the author.

Acknowledgements

This work was partially supported by the BASF SE. The authors acknowledge the support from the Karlsruhe Nano Micro Facility (KNMFi, www.knmf.kit.edu), a Helmholtz research infrastructure at Karlsruhe Institute of Technology (KIT, www.kit.edu). Dr. Thomas Bergfeldt and team (IAM-AWP, KIT) are acknowledged for performing the ICP-OES measurements. The authors are grateful to the Federal Ministry of Education and Research (Bundesministerium für Bildung und Forschung, BMBF) for funding within the project UNIKAM (03XP0484A, 03XP0484B).

Open access funding enabled and organized by Projekt DEAL.

Conflict of Interest

The authors declare no conflict of interest.

Data Availability Statement

The data that support the findings of this study are available from the corresponding author upon reasonable request.

Keywords

first-cycle capacity loss, ion exchange, Ni-rich cathode, point defects

Received: February 7, 2024
Revised: June 10, 2024
Published online:

[1] G. E. Blomgren, *J. Electrochem. Soc.* **2017**, *164*, A5019.
[2] W. Li, H. Y. Asl, Q. Xie, A. Manthiram, *J. Am. Chem. Soc.* **2019**, *141*, 5097.
[3] S. Schweidler, M. Bianchini, P. Hartmann, T. Brezesinski, J. Janek, *Batter. Supercaps* **2020**, *3*, 1021.
[4] K.-Y. Park, Y. Zhu, C. G. Torres-Castanedo, H. J. Jung, N. S. Luu, O. Kahvecioglu, Y. Yoo, J.-W. T. Seo, J. R. Downing, H.-D. Lim, M. J. Bedzyk, C. Wolverton, M. C. Hersam, *Adv. Mater.* **2022**, *34*, 2106402.
[5] L. de Biasi, A. O. Kondrakov, H. Geßwein, T. Brezesinski, P. Hartmann, J. Janek, *J. Phys. Chem. C* **2017**, *121*, 26163.
[6] H.-H. Ryu, B. Namkoong, J.-H. Kim, I. Belharouak, C. S. Yoon, Y.-K. Sun, *ACS Energy Lett.* **2021**, *6*, 2726.

[7] B. You, Z. Wang, F. Shen, Y. Chang, W. Peng, X. Li, H. Guo, Q. Hu, C. Deng, S. Yang, G. Yan, J. Wang, *Small Methods* **2021**, *5*, 2100234.
[8] U.-H. Kim, E.-J. Lee, C. S. Yoon, S.-T. Myung, Y.-K. Sun, *Adv. Energy Mater.* **2016**, *6*, 1601417.
[9] F. Lin, I. M. Markus, D. Nordlund, T.-C. Weng, M. D. Asta, H. L. Xin, M. M. Doeff, *Nat. Commun.* **2014**, *5*, 3529.
[10] H.-H. Ryu, N.-Y. Park, T.-C. Noh, G.-C. Kang, F. Maglia, S.-J. Kim, C. S. Yoon, Y.-K. Sun, *ACS Energy Lett.* **2021**, *6*, 216.
[11] M. Bianchini, M. Roca-Ayats, P. Hartmann, T. Brezesinski, J. Janek, *Angew. Chem., Int. Ed.* **2019**, *58*, 10434.
[12] D. Caurant, N. Baffier, B. Garcia, J. P. Pereira-Ramos, *Solid State Ionics* **1996**, *91*, 45.
[13] E. Rossen, C. D. W. Jones, J. R. Dahn, *Solid State Ionics* **1992**, *57*, 311.
[14] D. Goonetilleke, B. Schwarz, H. Li, F. Fauth, E. Suard, S. Mangold, S. Indris, T. Brezesinski, M. Bianchini, D. Weber, *J. Mater. Chem. A* **2023**, *11*, 13468.
[15] R. D. Shannon, *Acta Crystallogr.* **1976**, *A32*, 751.
[16] M. Bianchini, J. Wang, R. J. Clément, B. Ouyang, P. Xiao, D. Kitchaev, T. Shi, Y. Zhang, Y. Wang, H. Kim, M. Zhang, J. Bai, F. Wang, W. Sun, G. Ceder, *Nat. Mater.* **2020**, *19*, 1088.
[17] M. Bianchini, F. Fauth, P. Hartmann, T. Brezesinski, J. Janek, *J. Mater. Chem. A* **2020**, *8*, 1808.
[18] K. Hoang, M. Johannes, *Chem. Mater.* **2016**, *28*, 1325.
[19] P. Kurzhals, F. Riewald, M. Bianchini, H. Sommer, H. A. Gasteiger, J. Janek, *J. Electrochem. Soc.* **2021**, *168*, 110518.
[20] F. Riewald, P. Kurzhals, M. Bianchini, H. Sommer, J. Janek, H. A. Gasteiger, *J. Electrochem. Soc.* **2022**, *169*, 020529.
[21] Z. Cui, Z. Guo, A. Manthiram, *Adv. Energy Mater.* **2023**, *13*, 2203853.
[22] Y. Song, Y. Cui, L. Geng, B. Li, L. Ge, L. Zhou, Z. Qiu, J. Nan, W. Wu, H. Xu, X. Li, Z. Yan, Q. Xue, Y. Tang, W. Xing, *Adv. Energy Mater.* **2024**, *14*, 2303207.
[23] W. van den Bergh, L. Karger, S. Murugan, J. Janek, A. Kondrakov, T. Brezesinski, *ChemElectroChem* **2023**, *10*, 202300165.
[24] J. Langdon, A. Manthiram, *Energy Storage Mater.* **2021**, *37*, 143.
[25] R. Rueß, D. Gomboso, M. Ulherr, E. Trevisanello, Y. Ma, A. Kondrakov, T. Brezesinski, J. Janek, *J. Electrochem. Soc.* **2023**, *170*, 020533.
[26] A. Liu, N. Zhang, J. E. Stark, P. Arab, H. Li, J. R. Dahn, *J. Electrochem. Soc.* **2021**, *168*, 040531.
[27] L. Karger, D. Weber, D. Goonetilleke, A. Mazilkin, H. Li, R. Zhang, Y. Ma, S. Indris, A. Kondrakov, J. Janek, T. Brezesinski, *Chem. Mater.* **2023**, *35*, 648.
[28] L. Karger, S. Korneychuk, W. van den Bergh, S. L. Dreyer, R. Zhang, A. Kondrakov, J. Janek, T. Brezesinski, *Chem. Mater.* **2024**, *36*, 1497.
[29] Y.-h. Luo, Q.-l. Pan, H.-x. Wei, Y.-d. Huang, L.-b. Tang, Z.-y. Wang, Z.-j. He, C. Yan, J. Mao, K.-h. Dai, X.-h. Zhang, J.-c. Zheng, *Nano Energy* **2022**, *102*, 107626.
[30] J.-Y. Hwang, C. S. Yoon, I. Belharouak, Y.-K. Sun, *J. Mater. Chem. A* **2016**, *4*, 17952.
[31] C. Delmas, I. Saadoune, P. Dordor, *Mol. Cryst. Liq. Cryst. Sci. Technol. Sect. A. Mol. Cryst. Liq. Cryst.* **1994**, *244*, 337.
[32] W. Liu, P. Oh, X. Liu, M.-J. Lee, W. Cho, S. Chae, Y. Kim, J. Cho, *Angew. Chem. Int. Ed.* **2015**, *54*, 4440.
[33] D. Goonetilleke, A. Mazilkin, D. Weber, Y. Ma, F. Fauth, J. Janek, T. Brezesinski, M. Bianchini, *J. Mater. Chem. A* **2022**, *10*, 7841.
[34] H. Kim, Y. Kong, W. M. Seong, A. Manthiram, *ACS Appl. Mater. Interfaces* **2023**, *15*, 26585.
[35] H. Nguyen, R. Silverstein, A. Zaveri, W. Cui, P. Kurzhals, S. Sicolo, M. Bianchini, K. Seidel, R. J. Clément, *Adv. Funct. Mater.* **2023**, https://doi.org/10.1002/adfm.202306168.
[36] H. Li, W. Hua, X. Liu-Théato, Q. Fu, M. Desmau, A. Missyul, M. Knapp, H. Ehrenberg, S. Indris, *Chem. Mater.* **2021**, *33*, 9546.
[37] S. Indris, M. Scheuermann, S. M. Becker, V. Šepelák, R. Kruk, J. Suffner, F. Gyger, C. Feldmann, A. S. Ulrich, H. Hahn, *J. Phys. Chem. C* **2011**, *115*, 6433.
[38] H. Li, W. Hua, B. Schwarz, M. Etter, S. Mangold, G. Melinte, N. P. M. Casati, H. Ehrenberg, S. Indris, *Chem. Mater.* **2022**, *34*, 8163.
[39] L. Wang, A. Mukherjee, C.-Y. Kuo, S. Chakrabarty, R. Yemini, A. A. Dameron, J. W. DuMont, S. H. Akella, A. Saha, S. Taragin, H. Aviv, D. Naveh, D. Sharon, T.-S. Chan, H.-J. Lin, J.-F. Lee, C.-T. Chen, B. Liu, X. Gao, S. Basu, Z. Hu, D. Aurbach, P. G. Bruce, M. Noked, *Nat. Nanotechnol.* **2024**, *19*, 208.
[40] S. Oswald, H. A. Gasteiger, *J. Electrochem. Soc.* **2023**, *170*, 030506.
[41] D. Pritzl, T. Teufl, A. T. S. Freiberg, B. Strehle, J. Sicklinger, H. Sommer, P. Hartmann, H. A. Gasteiger, *J. Electrochem. Soc.* **2019**, *166*, A4056.
[42] M. Mock, M. Bianchini, F. Fauth, K. Albe, S. Sicolo, *J. Mater. Chem. A* **2021**, *9*, 14928.
[43] E. B. Quisbert, F. Fauth, A. M. Abakumov, M. Blangero, M. Guignard, C. Delmas, *Small* **2023**, *19*, 2300616.
[44] P. Xiao, N. Zhang, H. S. Perez, M. Park, arXiv **2023**, https://doi.org/10.48550/arXiv.2311.06140.
[45] M. E. Arroyo y de Dompablo, G. Ceder, *J. Power Sources* **2003**, *119–121*, 654.
[46] M. Yi, Z. Cui, H. Celio, A. Manthiram, *Chem. Mater.* **2023**, *35*, 9352.
[47] S. Sicolo, M. Sadowski, K. Vettori, M. Bianchini, J. Janek, *Chem. Mater.* **2023**, *36*, 492.
[48] H.-H. Ryu, K.-J. Park, C. S. Yoon, Y.-K. Sun, *Chem. Mater.* **2018**, *30*, 1155.
[49] H. Li, M. Cormier, N. Zhang, J. Inglis, J. Li, J. R. Dahn, *J. Electrochem. Soc.* **2019**, *166*, A429.
[50] C. Delmas, J. P. Pérès, A. Rougier, A. Demourgues, F. Weill, A. Chadwick, M. Broussely, F. Perton, P. Biensan, P. Willmann, *J. Power Sources* **1997**, *68*, 120.
[51] G. Kresse, J. Furthmüller, *Phys. Rev. B* **1996**, *54*, 11169.
[52] G. Kresse, J. Furthmüller, *Comput. Mater. Sci.* **1996**, *6*, 15.
[53] G. Kresse, D. Joubert, *Phys. Rev. B* **1999**, *59*, 1758.
[54] P. E. Blöchl, *Phys. Rev. B* **1994**, *50*, 17953.
[55] J. Klimeš, D. R. Bowler, A. Michaelides, *J. Phys. Condens. Matter* **2010**, *22*, 022201.
[56] J. L. Kaufman, J. Vinckevičiūtė, S. Krishna Kolli, J. Gabriel Goiri, A. Van der Ven, *Philos. Trans. R. Soc. A Math. Phys. Eng. Sci.* **2019**, *377*, 20190020.
[57] J. Vinckevičiūtė, M. D. Radin, N. V. Faenza, G. G. Amatucci, A. Van der Ven, *J. Mater. Chem. A* **2019**, *7*, 11996.
[58] M. D. Radin, J. C. Thomas, A. Van der Ven, *Phys. Rev. Mater.* **2020**, *4*, 043601.
[59] S. Sicolo, M. Mock, M. Bianchini, K. Albe, *Chem. Mater.* **2020**, *32*, 10096.
[60] A. Stukowski, *Model. Simul. Mater. Sci. Eng.* **2010**, *18*, 015012.